

Article

In Situ Utilization of Electron-Enhanced Degradation of Azo Dyes in a Constructed Wetland–Microbial Fuel Cell Coupling System

Xiangfeng Xie ^{1,2}, Jijing Hu ¹, Xian Cao ^{1,3}, Shuai Zhang ³, Takashi Sakamaki ⁴  and Xianning Li ^{1,*}¹ College of Energy and Environment, Southeast University, Nanjing 210096, China² Jiangsu Academy of Environmental Industry and Technology Corporation, Nanjing 211800, China³ Jiangsu Key Laboratory of Atmospheric Environment Monitoring and Pollution Control (AEMPC), Collaborative Innovation Center of Atmospheric Environment and Equipment Technology, Nanjing University of Information Science & Technology, Nanjing 210044, China⁴ Department of Civil and Environmental Engineering, Graduate School of Engineering, Tohoku University, Aoba Aramaki 6-6-06, Sendai 980-8579, Japan

* Correspondence: 101010377@seu.edu.cn

Abstract: In this study, a constructed wetland was coupled with a microbial fuel cell to establish a coupled system known as the constructed wetland–microbial fuel cell (CW–MFC), utilized for the treatment of X-3B azo dye wastewater at varying concentrations. Experimental results indicated that the anodic region made the primary contributions to the discoloration of azo dyes and COD removal, with a contribution rate of 60.9–75.8% for COD removal and 57.8–83.0% for the effectiveness of discoloration. Additionally, the role of plants in the constructed wetland area could achieve the removal of small molecular substances and further discoloration. In comparison to open-circuit conditions, under closed-circuit conditions the CW–MFC effectively degraded X-3B azo dye wastewater. Under an external resistance of 2000 Ω , a maximum COD removal rate of 60.0% and a maximum discoloration rate of 85.8% were achieved for X-3B azo dye at a concentration of 100 mg/L. Improvements in the treatment efficiency of X-3B dye wastewater were achieved by altering the external resistance. Under an external resistance of 100 Ω and an influent concentration of X-3B of 800 mg/L, the COD removal rate reached 78.6%, and the decolorization rate reached 85.2%. At this point, the CW–MFC exhibited a maximum power density of 0.024 W/m³ and an internal resistance of 99.5 Ω . Spectral analysis and GC–MS results demonstrated the effective degradation of azo dyes within the system, indicating azo bond cleavage and the generation of numerous small molecular substances. Microbial analysis revealed the enrichment of electrogenic microorganisms under low external resistance conditions, where *Geobacter* and *Trichococcus* were dominant bacterial genera under an external resistance of 100 Ω , playing crucial roles in power generation and azo dye degradation within the system.

Keywords: MFC; extracellular electron transfer; coupled system; constructed wetland; bioelectricity generation; azo dye



Citation: Xie, X.; Hu, J.; Cao, X.; Zhang, S.; Sakamaki, T.; Li, X. In Situ Utilization of Electron-Enhanced Degradation of Azo Dyes in a Constructed Wetland–Microbial Fuel Cell Coupling System. *Sustainability* **2024**, *16*, 3181. <https://doi.org/10.3390/su16083181>

Academic Editor: Andrea G. Capodaglio

Received: 26 February 2024

Revised: 28 March 2024

Accepted: 3 April 2024

Published: 10 April 2024



Copyright: © 2024 by the authors. Licensee MDPI, Basel, Switzerland. This article is an open access article distributed under the terms and conditions of the Creative Commons Attribution (CC BY) license (<https://creativecommons.org/licenses/by/4.0/>).

1. Introduction

With the rapid development of industrialization and urbanization, the discharge of large quantities of organic dye wastewater and its by-products from industrial production processes has become one of the significant challenges to water environmental quality [1,2]. Reactive Red X-3B azo dye is a type of dye widely used in industries such as textiles, printing and dyeing, and chemicals. The high-concentration discharge of it in wastewater not only threatens water quality but also poses potential hazards to aquatic ecosystems [3,4]. The aromatic ring structure and the presence of azo bonds in azo dyes endow them with a stable chemical structure, making them difficult to degrade biologically [5]. Therefore, the development of efficient and environmentally friendly technologies for dye wastewater treatment is urgently needed to achieve sustainable development of water resources [6].

Constructed wetlands (CW) and microbial fuel cells (MFC) represent innovative applications of wetland plants and microbial electrochemical technology in wastewater treatment. Constructed wetlands, by simulating the ecological processes of natural wetlands and leveraging the collective actions of plants, soil, and microorganisms, exhibit notable capabilities for organic matter removal [7,8]. Sethulekshmi et al. constructed a horizontal flow constructed wetland for treating textile dye wastewater, achieving a maximum discoloration rate of $72 \pm 2\%$ and COD removal rate of $85 \pm 3\%$ [9]. However, traditional constructed wetlands may face challenges in achieving high efficiency when dealing with complex organic wastewater [10]. In this context, the introduction of microbial fuel cells provides a novel approach to wastewater treatment. Microbial fuel cells, by utilizing microbial electron transfer between the anode and cathode, directly convert chemical energy from organic wastewater into electrical energy [11,12]. This technology not only achieves efficient wastewater degradation but also generates renewable electrical energy [13]. When applied to wastewater containing azo dyes, microbial fuel cells can efficiently degrade these organic dyes while simultaneously generating electricity [14–16]. Mousavian et al. constructed a dual-chamber microbial fuel cell with a graphite electrode modified by carbon nanotubes as the cathode. When the initial dye concentration was 80 mg/L, the decolorization efficiency of Reactive Blue 221 was 73.4% [17]; Chaijak et al. utilized *Enterobacter* sp. TS1L and textile dye wastewater to construct a dual-chamber microbial fuel cell system, achieving a decolorization rate of 72.96% for the dye wastewater [18]; Piskin et al. utilized a microbial fuel cell to treat azo dye wastewater and conducted response-surface optimization of reaction parameters. Under the optimal conditions, the removal efficiency of Sunfix Red S3B reached 91.26%, while the removal efficiency of COD was 21.61% [19]; Sun et al. studied the impact of anodic inoculants on azo dye discoloration in MFC, observing a 20.3% improvement in the decolorization of Congo Red azo dye when using textile dyeing sludge as an anodic inoculant [20].

The aim of this study is to achieve effective treatment of azo dye wastewater using sustainable technologies. Building upon prior research, we integrate shallow artificial wetlands with microbial fuel cells (CW–MFC). The role of wetland plants enhances the oxidation–reduction potential in the cathodic zone [21]. By leveraging the natural redox gradient of artificial wetlands, we establish a coupled system of artificial wetlands and microbial fuel cells [22]. This coupled system is then applied to the treatment of X-3B azo dye wastewater. By adjusting the different concentrations of X-3B and external resistance conditions, we investigate in depth the purification performance of this coupled system for azo dye wastewater under various environmental conditions. As a low-carbon, low-energy-consumption treatment technology that does not require external energy input and has the potential to generate electricity [23], the CW–MFC coupled system holds promise for wide application in real-world environments. It offers a new sustainable development pathway for addressing organic dye wastewater pollution issues.

2. Materials and Methods

2.1. Reactor Configuration

As shown in Figure 1, the primary body of the experimental setup was constructed using acrylic organic glass. It comprised a conical-shaped distributor at the bottom, a cylindrical main body, and an upper effluent weir. To simulate the actual conditions of shallow artificial wetlands, the apparatus chosen for this study has a relatively large diameter-to-height ratio. The column has an inner diameter of 30 cm, and the overall height of the reactor is 45 cm. The effective volume of the reactor was 7 L. The influent flowed in an upflow manner, sequentially passing through the bottom supporting layer, anode (activated carbon layer), intermediate gravel layer, and cathode (activated carbon layer). The gravel in the bottom supporting layer had a controlled particle size of 2–3 cm, while the gravel in the intermediate layer was controlled at 1–1.5 cm. The anode and cathode layers comprised granular activated carbon (average particle size of 4–6 mm) and stainless steel mesh (20 mesh). The granular activated carbon was washed with water, then soaked

separately in 1 mol/L NaOH and HCl for 24 h to remove any potential contaminants. The inoculated sludge was obtained from a wastewater treatment plant in Jiangning, Nanjing City, China. The cathode was an air cathode, and water spinach was planted in the cathode area as part of the constructed wetland. The cathode and anode were connected via titanium wires and external resistance, while the parts in contact with the solution were encapsulated with epoxy resin to prevent short circuits. Sampling ports were installed from bottom to top at the inflow area of the anode, outflow area of the anode, inflow area of the cathode, and the overflow weir for sampling the effluent from the cathode area.

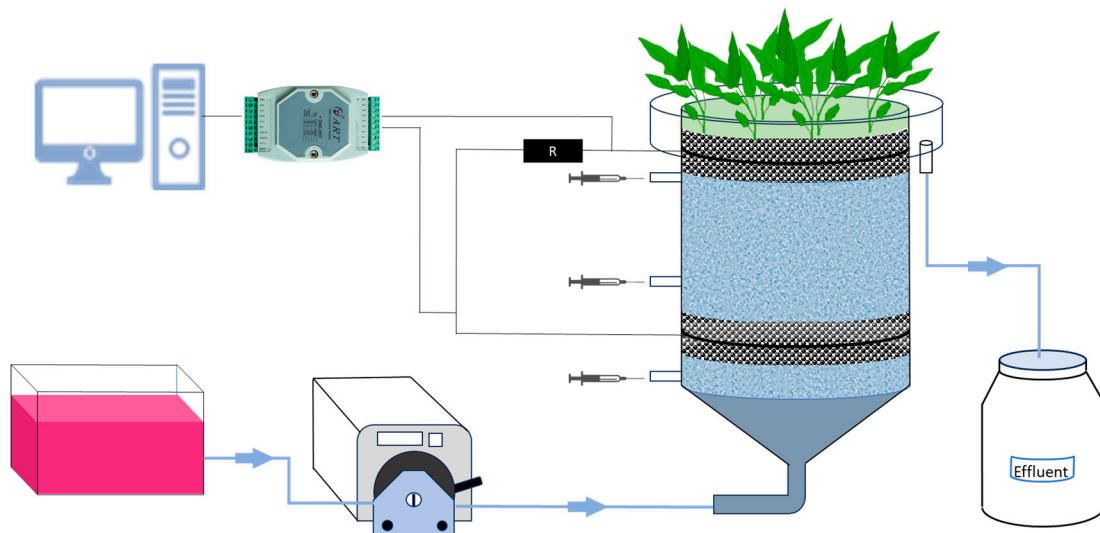


Figure 1. Structure of CW-MFC.

2.2. System Operation

Synthetic wastewater containing Reactive Red X-3B dye served as the influent in this experiment. Throughout the experimental period, the influent contained a glucose concentration of 500 mg/L. The nutrient and buffering solution formulations remained consistent with previous experiments [24]. The influent was delivered to the reactor's bottom distribution area via a peristaltic pump. System current was adjusted by modifying the external resistance. The hydraulic retention time (HRT) for the entire experiment was 2 days. After reactor initiation, acclimation was carried out under an external resistance of 2000 Ω . Daily monitoring of cathode and anode potentials occurred until stability was achieved, indicating successful initiation. The first set of experiments focused on evaluating the CW-MFC system's removal efficiency for different concentrations of X3-B. The second set delved into studying the purification efficacy of high-concentration X3-B dye wastewater under various current conditions. Finally, activated carbon without sludge inoculation was used as cathode and anode as an adsorption control experiment. After adsorption stabilization, the adsorption effect of cathodic and anodic activated carbon as well as of the matrix layer on X3-B dye wastewater was investigated.

2.3. Electrochemical Analysis

Voltage (V) and current (I) were recorded by the data acquisition module (DAM-3057 and DAM-3210, Art Technology Co., Ltd., Beijing, China) and automatically saved on a computer. At the conclusion of the experimental cycle, polarization curves were determined using the steady-state method. The coupled system was maintained in an open-circuit state for 12 h, and then the external resistance was varied using a variable resistor box within the range of 100,000 Ω to 5 Ω . After stabilizing for 30 min, the voltage across the variable resistor was measured, and the current was calculated using Ohm's law. Polarization curves were plotted with current as the abscissa and voltage as the ordinate. The slope of the linear segment represented internal resistance. Current density and unit anode volume

power density were calculated and plotted with current density on the abscissa and unit anode volume power density on the ordinate to form a power-density curve.

2.4. Other Analyses

Chemical oxygen demand (COD) was determined using the potassium dichromate method. For samples with concentrations exceeding the detection limit, further dilution was necessary for accurate measurement. X-3B concentration was measured using a UV-vis spectrophotometer (UV 9100B PC, LabTech, Los Angeles, CA, USA), detecting X-3B's maximum absorption peak at 538 nm. By referencing a standard curve plotted within the range of 0–100 mg/L, X-3B concentrations were obtained. Influent and effluent samples, after freeze-drying, underwent Fourier-transform infrared spectroscopy (FTIR) (Nicolet iS50, ThermoFisher, Waltham, MA, USA) for analyzing changes in dye structure and functional groups. Intermediate degradation products were analyzed using gas chromatography–mass spectrometry (GC–MS) (7890A, Agilent, Santa Clara, CA, USA). From the MFC outlet, a 300 mL sample was filtered through a 0.45 µm membrane. The sample was thrice extracted with chromatography-grade CH₂Cl₂. The extracts were transferred from the lower layer of a separation funnel to a rotary evaporator and evaporated at 40 °C (under a vacuum of 0.098–0.001 mPa) to approximately 4 mL. The sample was continuously concentrated via nitrogen blow until reaching a volume of 2 mL, then analyzed using GC–MS. The GC conditions utilized a db5 mass spectrometry quartz capillary column (φ 0.32 mm × 25 m), high-purity He carrier gas at a flow rate of 39.5 cm/s, an inlet temperature of 280 °C, a transfer line temperature of 280 °C, and a solvent delay time of 4 min. The column temperature started at 60 °C for 0.5 min, was ramped to 235 °C at 25 °C/min, held for 2 min, increased to 250 °C at 2 °C/min, held for 5 min, and finally raised to 280 °C at 15 °C/min for 5 min. The injection volume was 1 µL. MS operated in full-scan mode, using the electron-impact ionization mode with an electron energy of 70 eV, ion source temperature of 280 °C, electron multiplier voltage of 1605 V, and scanning range from 45–600 *m/z*. Scanning electron microscopy (SEM) (Supra55, Zeiss, Oberkochen, Germany) was employed to observe the morphology of the biofilm attached to the granular activated carbon on the anode.

For a more in-depth analysis of the microbial community on the MFC anode, genomic DNA was extracted from microbial samples on the anode of activated carbon. The DNA concentration was measured using a TBS-380, and DNA purity was assessed using a NanoDrop2000. DNA integrity was verified through 1% agarose gel electrophoresis. The V3-V4 hypervariable regions of the bacterial 16S rRNA genes were amplified in the ABI GeneAmp® 9700 PCR Thermocycler (Applied Biosystems, Foster City, CA, USA). PCR products were then extracted from a 2% agarose gel and purified using the AxyPrep DNA Gel Extraction Kit (Axygen Biosciences, Union City, CA, USA) according to the manufacturer's instructions. DNA quantification was performed using the Quantus™ Fluorometer (Promega, Madison, WI, USA). Libraries were constructed using the NEXTFLEX Rapid DNA-Seq Kit (Perkin Elmer, Waltham, MA, USA). Sequencing was carried out on the MiSeq PE300/Novaseq PE250 platforms (Illumina, San Diego, CA, USA).

3. Results and Discussion

3.1. Electricity Production Performance and Removal Efficiency

As shown in Figure 2, the operational cycle comprises three phases. Phase I is the initiation stage, during which the anodic electrogenic microorganisms gradually adapt to the environment. The anode potential decreases continuously, and the output voltage increases. After approximately 30 days of operation, the output voltage and current of each reactor stabilized, indicating successful startup. This suggests that shallow artificial wetlands can effectively couple with MFCs. In Phase II, the external resistance for all experimental setups is maintained at 2000 Ω. Control group A is set to an open circuit. Each experimental group is employed to treat X-3B azo dye wastewater at concentrations ranging from 100 mg/L to 800 mg/L. During Phase II, the output voltage of each experimental

group ranges between 400 mV and 500 mV, with the output current remaining relatively consistent at around 0.2 mA. In Phase III, the external resistance of each experimental group is altered to investigate further removal of high-concentration X-3B azo dye under different output current conditions. It can be observed that the output current of various experimental groups remains relatively stable throughout the testing period. Group F exhibits the highest output current, with an average of 1.01 mA, while Group B has the smallest output current, averaging 0.07 mA. Finally, the impact of current intensity on the anodic microbial community is assessed at the end of the testing period.

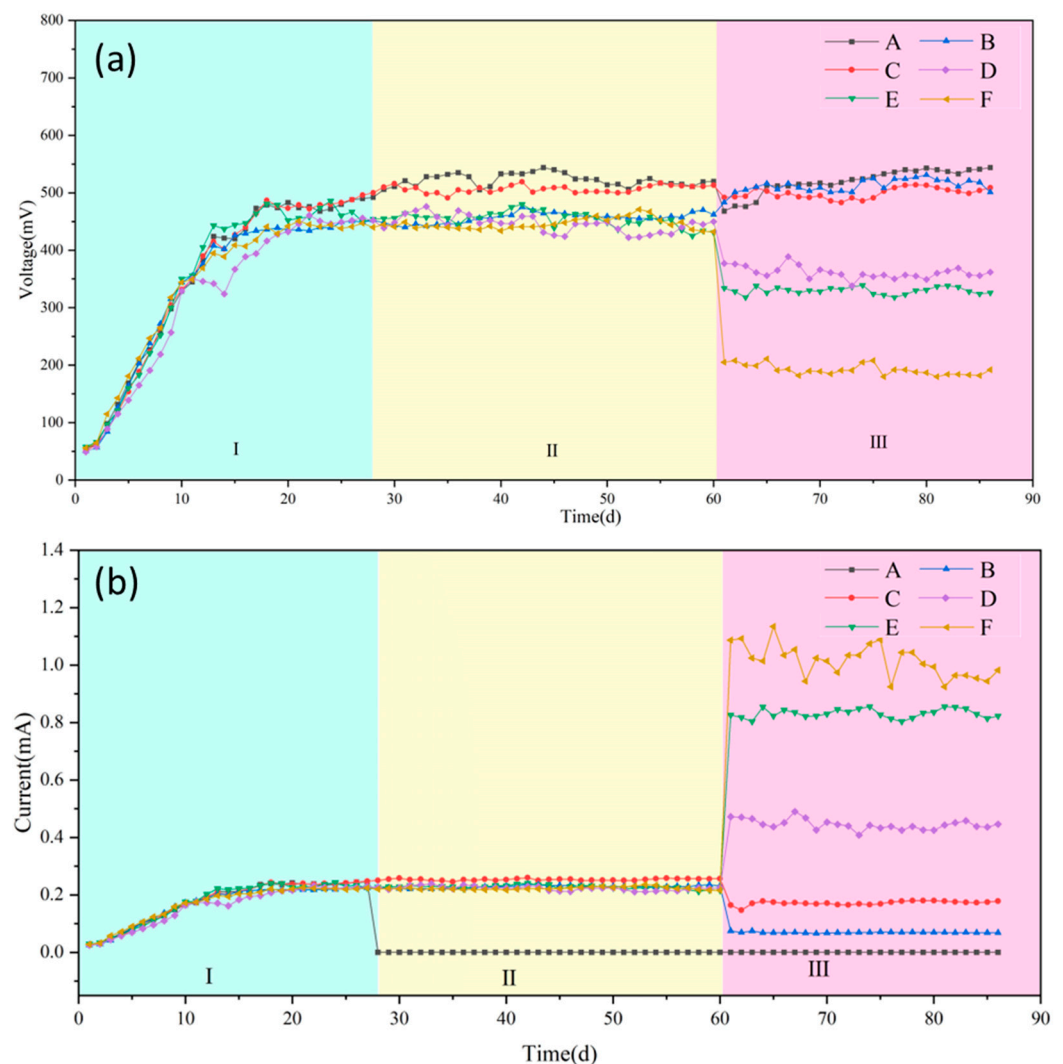


Figure 2. (a) Variations in output voltage of each device during the operational phase. (b) Variations in output current of each device during the operational cycle. A–F represent different experimental setups. Phase II: Device A (CK, 800 mg/L); Device B (2000 Ω , 100 mg/L); Device C (2000 Ω , 200 mg/L); Device D (2000 Ω , 400 mg/L); Device E (2000 Ω , 600 mg/L); Device F (2000 Ω , 800 mg/L). Phase III: Device A (CK, 800 mg/L); Device B (6000 Ω , 800 mg/L); Device C (2000 Ω , 800 mg/L); Device D (700 Ω , 800 mg/L); Device E (200 Ω , 800 mg/L); Device F (100 Ω , 800 mg/L).

Figure 3 displays the polarization curves and power-density curves of each device under varying external resistance conditions for the MFCs. As the external resistance of the MFCs increases, it is evident that the slope of the polarization curves for each reactor steadily rises. This suggests a positive correlation between the changes in internal resistance and external resistance for each reactor. The fitted results indicate that when the external resistances of the reactors are set to 100 Ω , 200 Ω , 700 Ω , 2000 Ω , and 6000 Ω , the corresponding internal resistances of the MFCs are 99.5 Ω , 229.4 Ω , 247.8 Ω , 838.1 Ω ,

and 1162 Ω , respectively. Notably, the open-circuit condition exhibits the highest internal resistance, fitted at 1177 Ω . Additionally, with the increase in MFC external resistance, there is a decreasing trend observed in the maximum power density for each reactor. The fitted results demonstrate that when the external resistances of the reactors are 100 Ω , 200 Ω , 700 Ω , 2000 Ω , and 6000 Ω , the maximum power densities of the MFCs are 0.024 W/m^3 , 0.023 W/m^3 , 0.022 W/m^3 , 0.007 W/m^3 , and 0.009 W/m^3 , respectively. Notably, the open-circuit condition shows the lowest maximum power density, fitted at 0.004 W/m^3 .

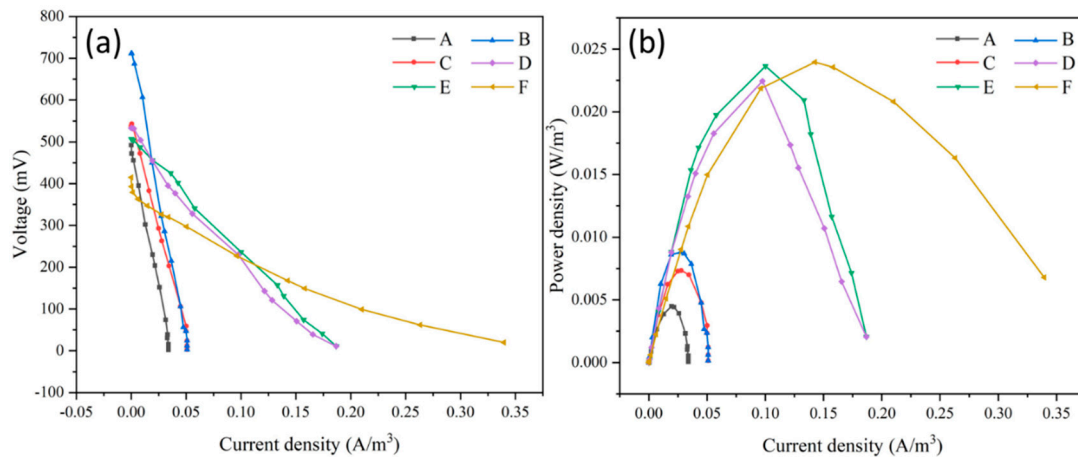


Figure 3. (a) Polarization curves of all devices at the end of the entire operational cycle. (b) Power-density curves.

Figure 4a,b illustrate the COD removal and decolorization rates of CW-MFC when handling different concentrations of X-3B. It can be observed that, as X-3B concentrations escalate from 100 mg/L to 800 mg/L, the average COD removal rate of CW-MFC shows a declining trend. This aligns with the findings of Rathour et al., that, as dye wastewater concentration increased from 10% to 90%, COD removal by CW-MFC declined from $97.73 \pm 1.61\%$ to $70 \pm 2\%$ [25]. In this study, the maximum average COD removal rate was achieved when treating X-3B azo dye at a concentration of 100 mg/L, approximately 60.1%, which was significantly different from other experimental groups. The average COD removal rates for X-3B azo dye concentrations, ranging from 200 mg/L to 800 mg/L, varied between 49.2% and 54.1%, with no significant differences observed between groups. Additionally, when treating X-3B azo dye at a concentration of 800 mg/L, the average COD removal rate under closed-circuit conditions was 50.0%, while under open-circuit conditions it was only 35.8%, indicating a significant difference.

Similarly, the average decolorization rate of CW-MFC decreased continuously with increasing X-3B concentration. The experimental group with X-3B concentration at 100 mg/L exhibited the highest average decolorization rate, approximately 85.8%, significantly higher than other experimental groups. Conversely, the experimental group with X-3B concentration at 800 mg/L showed the lowest average decolorization rate, approximately 64.9%, while the average decolorization rate for the open-circuit control group was only 61.2%, showing significant differences from all experimental groups.

Figure 4c,d demonstrate the contribution of the adsorption effect of the cathodic and anodic region activated carbon to the decolorization of X-3B and COD removal. Under different concentration conditions, the adsorption effect exhibited similar effects on both X-3B decolorization and COD removal. The contribution of the anodic adsorption effect to COD removal and X-3B decolorization ranged from 6.5% to 7.7% and 13.1% to 16.8%, respectively. Similarly, the contribution of the cathodic adsorption effect to COD removal and X-3B decolorization ranged from 8.8% to 12.2% and 6.5% to 9.2%, respectively.

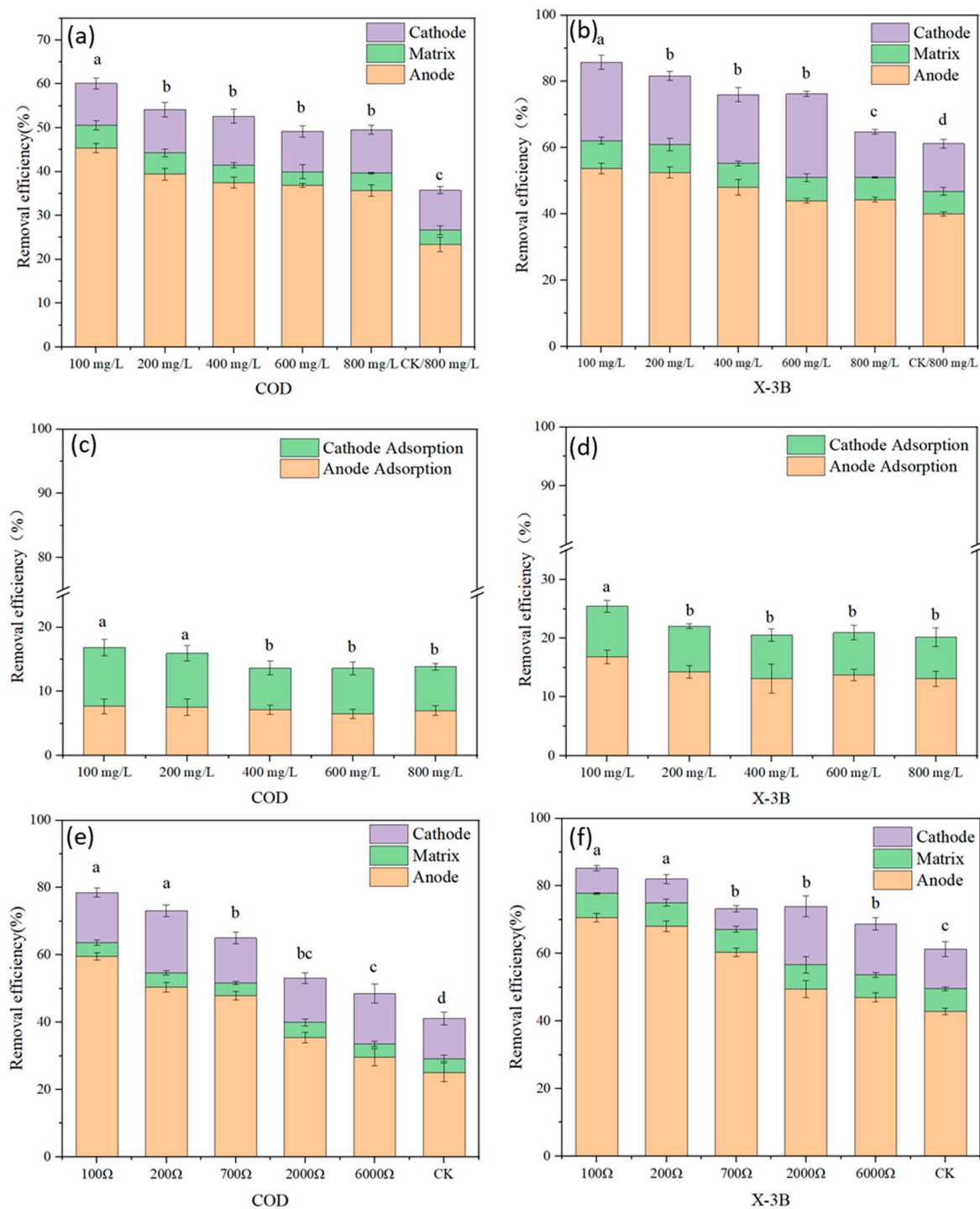


Figure 4. (a) Contribution of different zones to COD removal when treating various concentrations of X-3B with CW-MFC. (b) Contribution of different zones to azo dye decolorization when treating different concentrations of X-3B with CW-MFC. (c) Contribution of adsorption by cathodic and anodic activated carbon to COD removal when treating different concentrations of X-3B with CW-MFC. (d) Contribution of adsorption by cathodic and anodic activated carbon to azo dye decolorization when treating different concentrations of X-3B with CW-MFC. (e) Contribution of different zones to COD removal when treating 800 mg/L of X-3B under different external resistance conditions with CW-MFC. (f) Contribution of different zones to azo dye decolorization when treating 800 mg/L of X-3B under different external resistance conditions with CW-MFC. (Different letters represent significant differences between groups).

Figure 4e,f depict the COD removal and decolorization rates of CW-MFC when handling 800 mg/L X-3B under various current conditions. It can be observed that with decreasing output current in experimental groups, CW-MFC's average COD removal rate substantially decreased. The group with an external resistance of 100 Ω exhibited the highest average COD removal and decolorization rates, reaching 78.6% and 85.2%, respectively, significantly higher than other groups. With CW-MFC external resistance varying between 200 Ω and 6000 Ω , the average COD removal rates ranged from 48.5% to 73.2%, while the decolorization rates ranged from 68.8% to 82.0%. Furthermore, under open-circuit conditions, CW-MFC exhibited the lowest average COD removal rate and decolorization rate for 800 mg/L X-3B azo dye wastewater, at 41.1% and 61.3%, respectively, significantly different from other experimental groups.

Overall, the anodic region exhibits higher COD removal and decolorization efficiency, with a contribution rate of 60.9–75.8% for COD removal and 57.8–83.0% for decolorization. As the concentration of azo dye increases, the effectiveness of pollutant removal in the anodic region decreases, consistent with the overall removal rate trend. The matrix layer under different conditions demonstrates similar adsorption capacities, with contribution rates of 5.2–10.0% for COD removal and 8.4–11.1% for decolorization. The cathodic CW area exhibited nearly consistent COD removal efficiency across different wastewater concentrations, with no noticeable pattern in its contribution to decolorization rates. Li et al. constructed a dual-chamber MFC system and separately investigated the removal efficiency of X-3B in the cathodic and anodic regions. Under optimal voltage conditions, the cathode exhibited a decolorization rate of only 0–14.16% [26]. Thung et al. provided the cathode with electron acceptors through aeration, resulting in a COD removal rate of less than 10% [27]. Compared to these studies, the cathodic region in our research demonstrated better COD removal rates (9.6–18.5%) and decolorization rates (6.1–25.2%), slightly higher than the results of adsorption experiments. The enhancement in decolorization ability of this region may be attributed to the combined adsorption of wetland plants and activated carbon particles in the CW region [28,29]. The effectiveness of COD removal may result from the combined action of activated carbon adsorption and wetland plant degradation in the cathodic region. Compared to traditional MFCs, CW-MFCs utilize artificial wetlands as the cathode, taking advantage of the aerobic environment formed by wetland plant root oxygen release without the need for cathodic aeration [30], which can expand the application range of this technology.

3.2. Intermediates and Degradation Pathways

Figure 5a,b display the FTIR spectra of the inlet and outlet of CW-MFC when treating different concentrations of X-3B azo dye wastewater, as well as the FTIR spectra of the inlet and outlet of CW-MFC under various external resistance conditions when treating X-3B azo dye wastewater. A broad absorption peak is observed around 3460 cm^{-1} , representing the stretching vibrations of O-H and N-H [31,32]; two absorption peaks at 2336 cm^{-1} and 2362 cm^{-1} correspond to characteristic absorption peaks of CO_2 . The absorption peak at 1650 cm^{-1} corresponds to the $-\text{N}=\text{N}-$ structure of azo dyes [33,34]. A series of sharp absorption peaks in the range of 1650 cm^{-1} to 1539 cm^{-1} represent skeletal vibrations of benzene rings, naphthalene rings, triazine structures, as well as stretching vibrations of functional groups such as C=N, C=C, and N=O [33,35]. The absorption peak near 1040 cm^{-1} corresponds to R-SO₃- [36].

Comparing the cathode outlet with the inlet, a notable decrease in the absorption peak at 1650 cm^{-1} is observed in all devices, indicating the cleavage of the $-\text{N}=\text{N}-$ of azo dyes. Correspondingly, an increase in the intensity of the skeletal vibration absorption peaks of benzene rings, naphthalene rings, and triazine structures is noticed, suggesting the formation of some smaller molecular structures after azo bond cleavage [37].

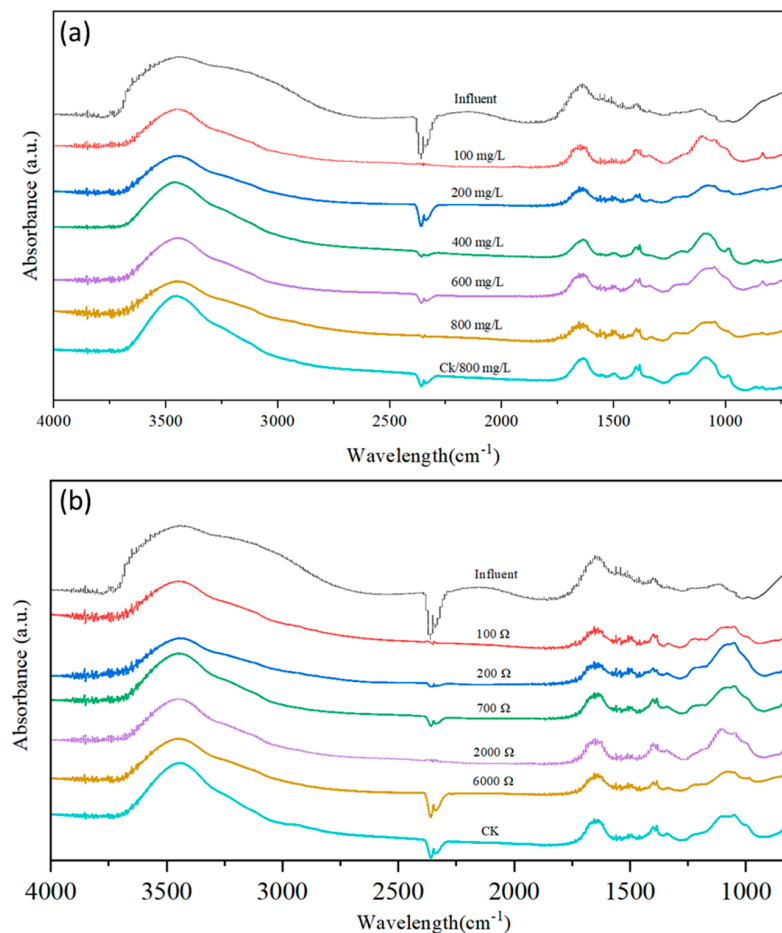


Figure 5. (a) FTIR profiles of influent and effluent effluents treated with different concentrations of X-3B azo dyes by CW-MFC. (b) FTIR patterns of influent and effluent treated with X-3B azo dye wastewater by CW-MFC under different external resistance conditions.

Figure 6a illustrates the UV-vis full-spectrum scanning spectra of the inlet, anode, and cathode effluents of CW-MFC treating X-3B azo dye wastewater. X-3B exhibits five distinctive absorption peaks within the UV-visible range at 233 nm, 283 nm, 330 nm, 513 nm, and 538 nm. The peak at 233 nm corresponds to the benzene ring structure [38,39], the peak at 283 nm corresponds to the triazine structure [40], the peak at 330 nm corresponds to the naphthalene ring structure [41], and the broad absorption peak at 513 nm–538 nm is associated with the conjugated N- π structure [42], related to the $-N=N-$ structure of the X-3B azo dye and its chromophore.

It can be observed that the absorption peaks at 513 nm to 538 nm in both anode and cathode effluents are significantly lower than those in the influent, indicating the degradation of the X-3B conjugated N- π structure within the CW-MFC system, corresponding to the reason for the decolorization of the azo dye. Compared to the influent, a decrease in absorption peaks in all bands in the cathode effluent indicates the disruption of not only the conjugated structure of large molecules but also effective degradation of smaller molecules such as benzene rings and triazines in the cathodic layer. In comparison to the anode effluent, a decrease in the absorption peaks at 513 nm to 538 nm, and an increase at 233 nm and 283 nm, indicates degradation of the X-3B conjugated N- π structure in the cathodic area of the CW-MFC, generating intermediates containing benzene rings and triazine structures. However, these intermediates are not fully removed in the cathode area, leading to the presence of a certain COD concentration in the effluent, indicating that the cathode region of the CW-MFC is more effective in decolorization than in COD removal, consistent with the results shown in Figure 4a,b.

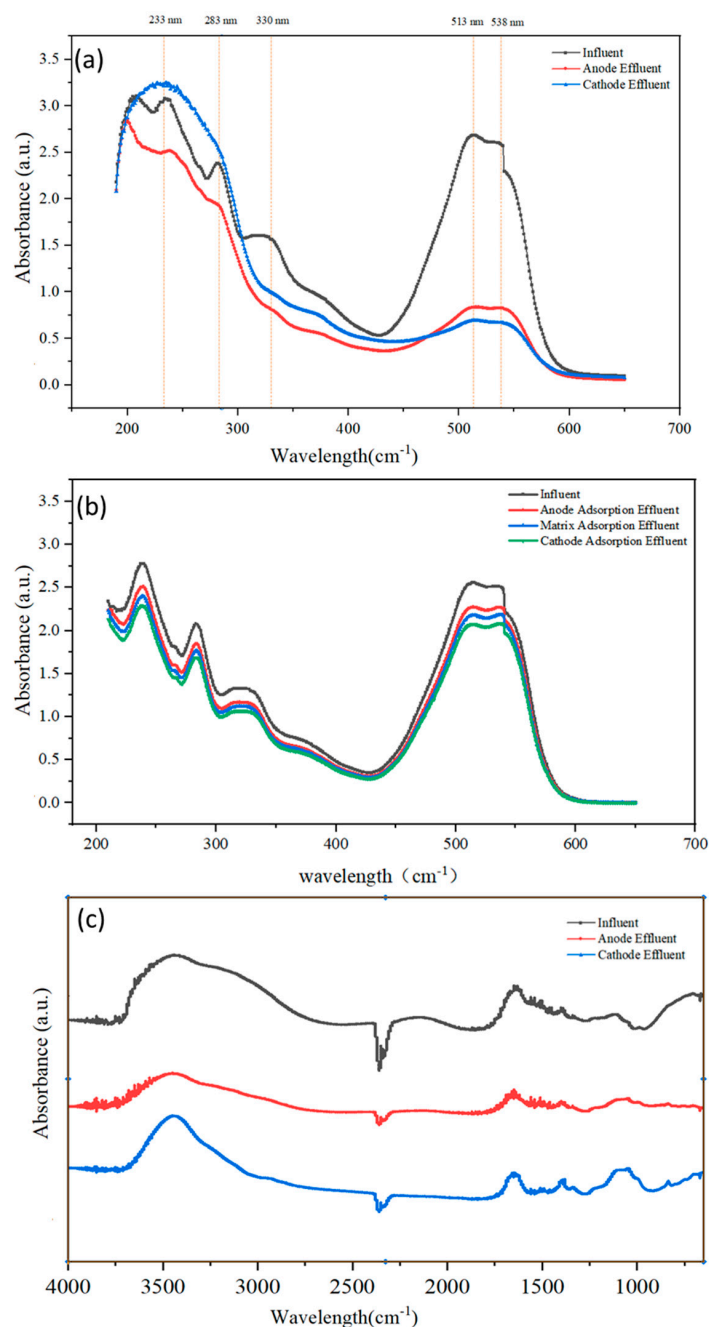


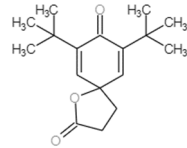
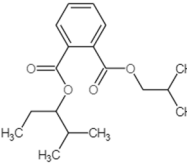
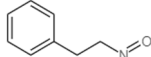
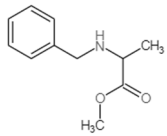
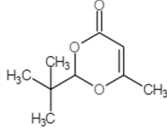
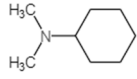
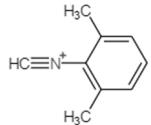
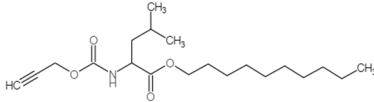
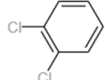
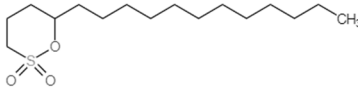
Figure 6. (a) CW-MFC influent, anode effluent, and cathode effluent UV-visible full-spectrum scan. (b) CW-MFC influent, anode adsorption effluent, matrix layer adsorption effluent and cathode adsorption effluent UV-visible full spectrum scan. (c) CW-MFC influent, anode effluent, and cathode effluent FTIR spectra.

Figure 6b illustrates the UV-vis full-spectrum scan of the adsorption control experiment. The experimental results further indicate that both the cathodic and anodic activated carbon, as well as the substrate region acting as the supporting layer, can achieve slight adsorption of X-3B. Additionally, the spectra of effluents from different regions only show a decrease in intensity, with no changes in waveform, suggesting that the adsorption effect does not disrupt the molecular structure of X-3B.

Figure 6c displays the FTIR spectra of the inlet, anode effluent, and cathode effluent of the CW-MFC, further corroborating the gradual reduction in the -N=N- intensity of the X-3B azo dye after passing through both anode and cathode, and an increase

in the skeletal vibration absorption peaks of benzene rings, naphthalene rings, and triazine structures after passing through the cathode, consistent with the UV results. To further identify the intermediate products of X-3B degradation, GC-MS analysis was conducted on the CW-MFC effluent at the end of different current-test periods. A total of twelve intermediate products of X-3B were detected, as shown in Table 1. These include ketones (C₁₇H₂₄O₃, C₉H₁₄O₃, C₁₀H₂₀O), amines (C₈H₁₇N, C₇H₁₄N₂), esters (C₁₈H₂₆O₄, C₉H₉NO, C₁₁H₁₅NO₂, C₂₀H₃₅NO₄), and other intermediates (C₉H₉N, C₆H₄Cl₂, C₁₆H₃₂O₃S).

Table 1. X-3B degradation intermediates.

Serial Number	Molecular Formula	Structural Formula
1	C ₁₇ H ₂₄ O ₃	
2	C ₁₈ H ₂₆ O ₄	
3	C ₉ H ₉ NO	
4	C ₁₁ H ₁₅ NO ₂	
5	C ₉ H ₁₄ O ₃	
6	C ₈ H ₁₇ N	
7	C ₉ H ₉ N	
8	C ₂₀ H ₃₅ NO ₄	
9	C ₆ H ₄ Cl ₂	
10	C ₁₆ H ₃₂ O ₃ S	

3.3. Microbial Community Composition

Figure 8 illustrates scanning electron microscope (SEM) images of the surface of the original granular activated carbon and the granular activated carbon retrieved from the anode region after the operational cycle. The original granular activated carbon exhibits a surface filled with pores of approximately 15 μm , 2 μm , and 0.2 μm , providing numerous attachment sites for electrogenic microorganisms [44]. After the operational cycle, evident microbial clusters are observed on the surface of the activated carbon, forming biofilm-like structures in the locations of the original larger pores. These microbial clusters exhibit abundant sticky substances secreted by bacteria, enhancing interconnection and impact resistance between microbial clusters. Additionally, this biofilm structure plays a crucial role in extracellular electron transfer, facilitating enhanced electron transfer and power generation between electrogenic microorganisms and the anode [45,46].

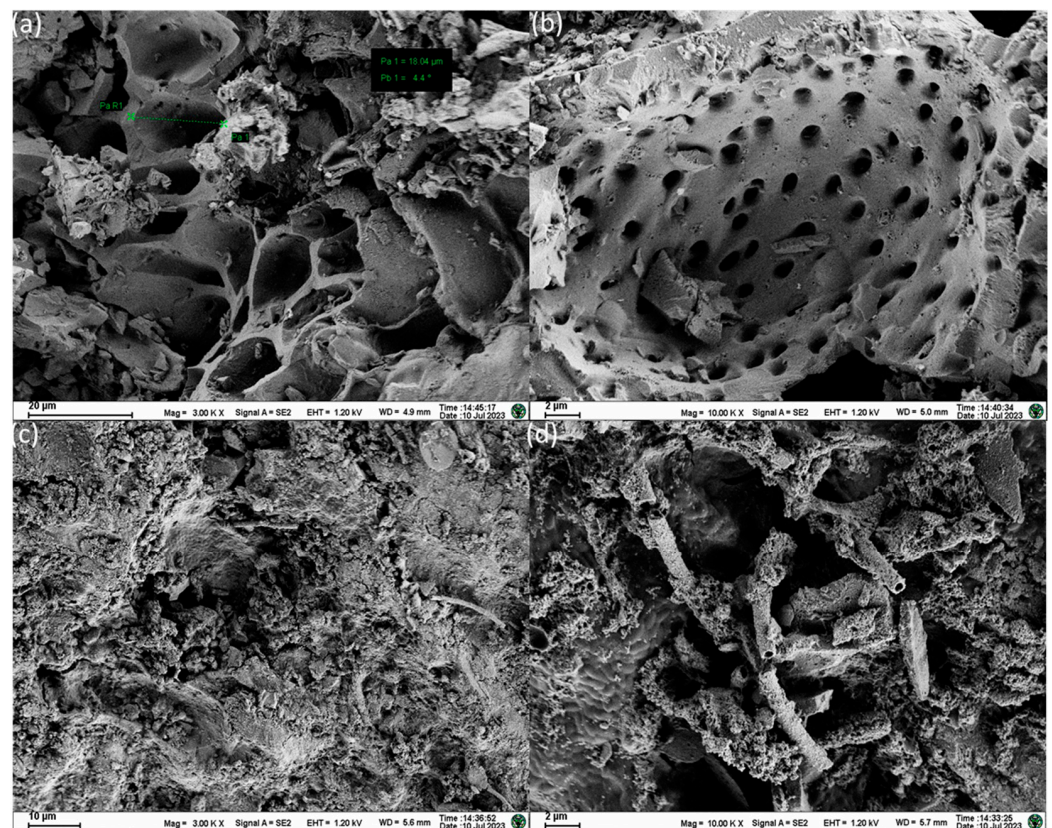


Figure 8. (a) SEM image of the original activated carbon at 3000 \times magnification. (b) SEM image of the original activated carbon at 10,000 \times magnification. (c) SEM image of the anode activated carbon at 3000 \times magnification. (d) SEM image of the anode activated carbon at 10,000 \times magnification.

Figure 9a,b illustrate the differences in the anodic microbial community at the phylum and genus levels under different conditions. At the phylum level, an analysis was conducted on the top 15 relatively abundant phyla, including Proteobacteria, Patescibacteria, Firmicutes, Bacteroidota, Chloroflexi, Desulfobacterota, Actinobacteriota, Acidobacteriota, Nitrospirota, Campilobacterota, Planctomycetota, Myxococcota, Gemmatimonadota, Verucomicrobiota, and unclassified. Compared to the original inoculum, the abundance of Proteobacteria significantly increased in both the control and experimental groups. Typically, anodic microbial communities in microbial fuel cells are primarily dominated by Proteobacteria [47], which display electrochemical activity. Furthermore, Proteobacteria are associated with the biodegradation of recalcitrant organic compounds [48], explaining the observed increase in their abundance in both the control and experimental groups. Patescibacteria, which was the dominant phylum in the original inoculum with an abun-

dance of 36.34%, is believed to participate in denitrification processes [49], and its abundance notably decreased in both the experimental and control groups. Firmicutes are also commonly found EAB bacteria [50,51], involved in extracellular electron transfer, with abundances ranging from 11.33% to 11.59% in all experimental and control groups. An increased abundance of Chloroflexi was observed in both the experimental and control groups, and previous studies suggest that Chloroflexi can degrade recalcitrant pollutants under anaerobic conditions [52], which might explain the increase in its abundance. Desulfobacterota, known to host numerous electroactive microorganisms [53], usually highly enrich at MFC anodes. In this experiment, the abundance of Desulfobacterota increased with higher external circuit currents. In the original inoculum, the abundance of Desulfobacterota was only 0.28%. However, under CK, I-min, and I-max conditions, the abundance of Desulfobacterota escalated to 8.78%, 13.70%, and 23.57%, respectively, indicating that lower external resistance conditions favor Desulfobacterota enrichment.

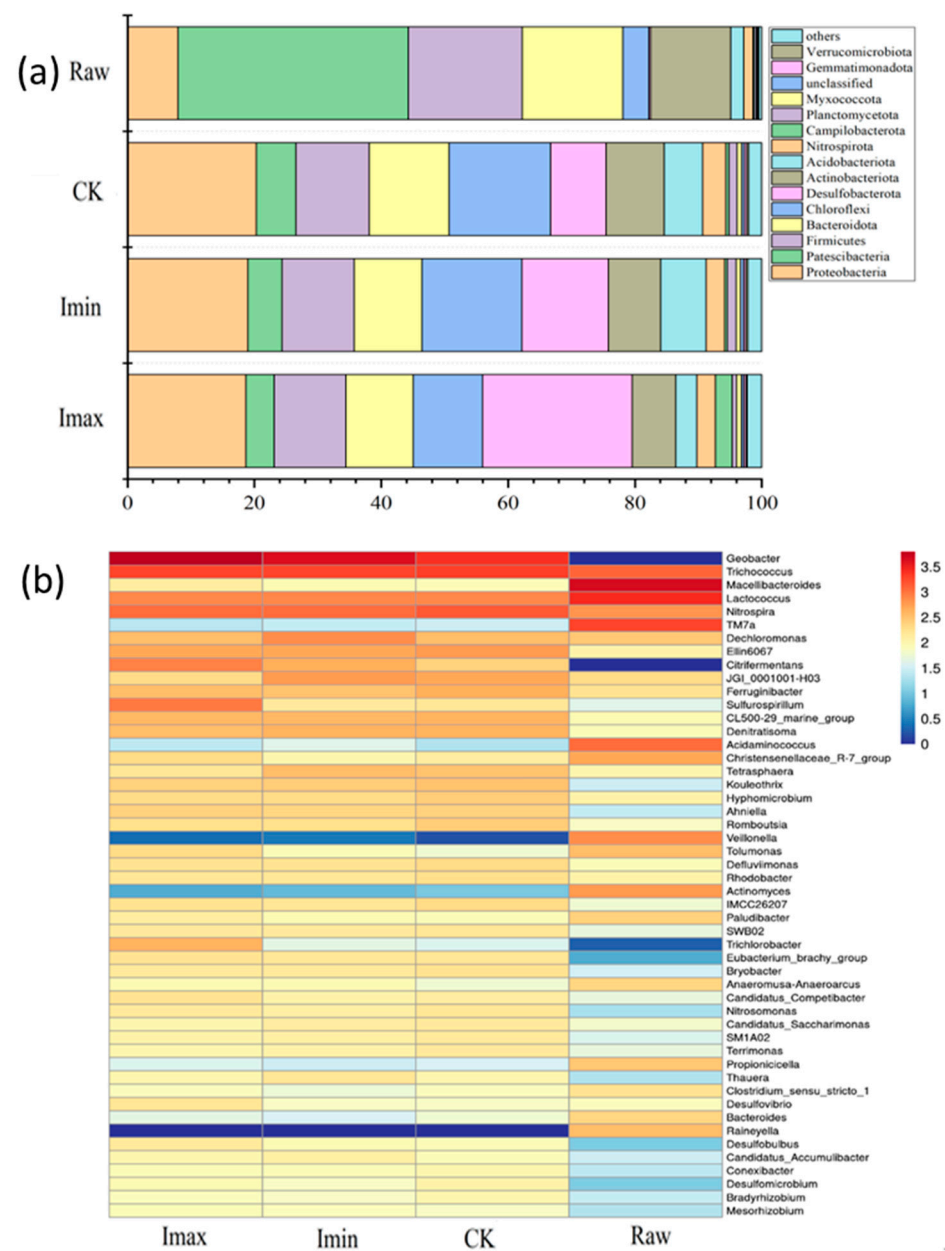


Figure 9. (a) Compositional variances in the anodic microbial community at the phylum level under different external resistance conditions, and (b) compositional differences of the top 50 anodic microbial communities at the genus level under different external resistance conditions.

At the genus level, the higher-abundance microbes in the experimental group include *Geobacter*, *Trichococcus*, *Lactococcus*, *Nitrospira*, and *Citrifermentans*. *Geobacter*, an important electrogenic microorganism, exhibited a negative correlation between its relative abundance in different reactors and the external resistance. Its abundance was 30.23%, 22.17%, and 14.46% under minimum external resistance, maximum external resistance, and CK conditions, respectively. *Geobacter* was hardly detected in the original water sample. According to Rago et al., the relatively higher current intensity resulting from lower external resistance is related to the extracellular electron transfer capability of *Geobacter* [54]. *Trichococcus*, belonging to the phylum Deinococcus, showed a minor variation in abundance across the experimental groups but had a slightly increased abundance compared to the original inoculum. *Trichococcus* possesses the capability to degrade various complex organic compounds into simpler molecules [55]; Guo et al. suggested that *Trichococcus* can facilitate the degradation of methyl orange in an MFC setup [56]. *Lactococcus*, an electroactive microorganism, is involved in fermentation and electricity generation at the MFC anode [57], aiding in the degradation of recalcitrant organic compounds [58]. Additionally, *Lactococcus* acts as a dye decolorizing agent [59]. Ravadelli et al. employed an anoxic–oxic membrane bioreactor (A/O-MBR) to treat wastewater containing azo dyes, and sequencing results demonstrated that *Lactococcus* is capable of degrading and decolorizing azo dyes [60]. *Nitrospira*, a nitrifying bacterium, oxidizes nitrites to nitrates, contributing to improved denitrification rates and promoting bioelectricity generation [61]; it was enriched in the experimental groups. *Citrifermentans*, another electrogenic microorganism, forms biofilms on carbon materials and participates in extracellular electron transfer processes [62]. Similarly to *Geobacter*, the abundance of *Citrifermentans* exhibited a negative correlation with external resistance in the setup.

3.4. Mechanism Analysis

In this study, the X-3B azo dye wastewater, after passing through the anodic region of the CW–MFC, underwent a combined effect of anaerobic conditions and bioelectrochemical processes. This environment led to the cleavage of azo bonds, facilitating significant decolorization and COD removal. High-molecular-weight dye molecules were degraded into smaller molecules such as ketones and esters due to the anaerobic conditions and bioelectrochemical interactions in the anodic zone. These smaller molecules subsequently flowed to the cathodic zone where further removal occurred through aerobic degradation, and absorption by plant roots, activated carbon particles, and the matrix. Microbial analysis indicated the enrichment of a significant number of microorganisms in the anodic region associated with electricity generation and azo dye degradation. As the external resistance of the system decreased, the increase in external circuit current further stimulated the enrichment of anodic electrogenic bacteria. Following direct and indirect extracellular electron transfer processes, electrons transferred from the intracellular space of electrogenic bacteria to the extracellular environment [63]. The additional electrons promoted the reduction degradation of the azo dye, hence enhancing the treatment efficiency of high-concentration dye wastewater by controlling the external resistance.

4. Conclusions

This study constructed a shallow-water-layer CW–MFC system, taking into account the effects of external resistance variation and pollutant concentration on the coupled system. Through pollutant concentration detection, UV-visible spectroscopy analysis, FTIR testing, and other methods, the contributions of different regions to pollutant removal were evaluated. Additionally, the final fate of X-3B within the coupled system was assessed by combining GC–MS results. The biological anode in the coupled system primarily contributes to the degradation of azo dyes, while the cathode further aids in decolorization through mechanisms such as adsorption. Microbial community analysis revealed that under low external resistance conditions, the enrichment of electroactive microorganisms such as *Geobacter* and *Lactococcus* at the anode of CW–MFC, as well as microorganisms

closely related to azo dye decolorization, such as *Trichococcus*, is more favorable. This can effectively improve the electrochemical performance of the system and enhance the decolorization and COD removal efficiency of the coupled system for azo dye wastewater.

Author Contributions: Methodology, X.X.; investigation, J.H.; resources, S.Z. and T.S.; writing—original draft, X.X.; writing—review & editing, X.C. and X.L.; funding acquisition, X.C. and X.L. All authors have read and agreed to the published version of the manuscript.

Funding: This work was supported by the National Natural Science Foundation of China (42077108 and 42377020), Jiangsu Provincial Innovation and Entrepreneurship Doctor Program (JSSCBS20210054), Open fund by Jiangsu Key Laboratory of Atmospheric Environment Monitoring and Pollution Control (KHK 2212).

Data Availability Statement: The datasets used and/or analyzed during the current study are available from the corresponding author upon reasonable request.

Conflicts of Interest: Xiangfeng Xie was employed by the Jiangsu Academy of Environmental Industry and Technology Corp. The remaining authors declare that the research was conducted in the absence of any commercial or financial relationships that could be construed as a potential conflict of interest.

References

1. Verma, P.; Samanta, S.K. Microwave-enhanced advanced oxidation processes for the degradation of dyes in water. *Environ. Chem. Lett.* **2018**, *16*, 969–1007. [[CrossRef](#)]
2. Zhang, C.; Chen, H.; Xue, G.; Liu, Y.; Chen, S.; Jia, C. A critical review of the aniline transformation fate in azo dye wastewater treatment. *J. Clean. Prod.* **2021**, *321*, 128971. [[CrossRef](#)]
3. Su, L.; Fan, X.; Yin, T.; Chen, H.; Lin, X.; Yuan, C.; Fu, D. Increasing power density and dye decolorization of an X-3B-fed microbial fuel cell via TiO₂ photocatalysis pretreatment. *RSC Adv.* **2015**, *5*, 83906–83913. [[CrossRef](#)]
4. Cheng, G.; Zhang, Y.; Sun, L.; Wan, J.; Li, Z.; Dang, C.; Fu, J. Enhanced degradation of reactive brilliant red X-3B by photocatalysis integrated with micro-electrolysis. *Environ. Sci. Pollut. Res.* **2021**, *28*, 49899–49912. [[CrossRef](#)] [[PubMed](#)]
5. Chen, L.; Jiang, L.; Gao, Y.; Pan, S.; Luan, H.; Zhang, G.; Xu, L.; Wang, M. Kinetic analysis of electron transfer process in decolorization of azo dyes by *Shewanella* combined with porous organic polymers in MFCs. *Int. J. Hydrogen Energy* **2024**, *52*, 1081–1091. [[CrossRef](#)]
6. Meng, F.; Yu, L.; Song, B.; Zhao, Y.; Zhi, Z.; Lin, C.; Song, M. Insights into the mechanism of redox pairs and oxygen vacancies of Fe₂O₃@CoFe₂O₄ hybrids for efficient refractory organic pollutants degradation. *Chemosphere* **2022**, *291*, 133069. [[CrossRef](#)] [[PubMed](#)]
7. McCorquodale-Bauer, K.; Grosshans, R.; Zvomuya, F.; Cicek, N. Critical review of phytoremediation for the removal of antibiotics and antibiotic resistance genes in wastewater. *Sci. Total Environ.* **2023**, *870*, 161876. [[CrossRef](#)]
8. Varma, M.; Gupta, A.K.; Ghosal, P.S.; Majumder, A. A review on performance of constructed wetlands in tropical and cold climate: Insights of mechanism, role of influencing factors, and system modification in low temperature. *Sci. Total Environ.* **2021**, *755*, 142540. [[CrossRef](#)]
9. Sethulekshmi, S.; Chakraborty, S. Textile wastewater treatment using horizontal flow constructed wetland and effect of length of flow in operation efficiency. *J. Environ. Chem. Eng.* **2021**, *9*, 106379. [[CrossRef](#)]
10. Li, X.; Cheng, M.; Jiao, X.; Zhao, Z.; Zhang, Y.; Gao, X. Advances in microbial electrochemistry-enhanced constructed wetlands. *World J. Microbiol. Biotechnol.* **2022**, *38*, 239. [[CrossRef](#)]
11. Xie, T.; Jing, Z.; Hu, J.; Yuan, P.; Liu, Y.; Cao, S. Degradation of nitrobenzene-containing wastewater by a microbial-fuel-cell-coupled constructed wetland. *Ecol. Eng.* **2018**, *112*, 65–71. [[CrossRef](#)]
12. Yan, X.; Lee, H.-S.; Li, N.; Wang, X. The micro-niche of exoelectrogens influences bioelectricity generation in bioelectrochemical systems. *Renew. Sustain. Energy Rev.* **2020**, *134*, 110184. [[CrossRef](#)]
13. Li, J.; Li, H.; Zheng, J.; Zhang, L.; Fu, Q.; Zhu, X.; Liao, Q. Response of anodic biofilm and the performance of microbial fuel cells to different discharging current densities. *Bioresour. Technol.* **2017**, *233*, 1–6. [[CrossRef](#)]
14. Li, Y.; Yang, H.-Y.; Shen, J.-Y.; Mu, Y.; Yu, H.-Q. Enhancement of azo dye decolorization in a MFC-MEC coupled system. *Bioresour. Technol.* **2016**, *202*, 93–100. [[CrossRef](#)] [[PubMed](#)]
15. Surti, P.; Kailasa, S.K.; Mungray, A.K. Enhancement of electrode properties using carbon dots functionalized magnetite nanoparticles for azo dye decolorization in microbial fuel cell. *Chemosphere* **2023**, *313*, 137601. [[CrossRef](#)]
16. Li, R.; Li, T.; Wan, Y.; Zhang, X.; Liu, X.; Li, R.; Pu, H.; Gao, T.; Wang, X.; Zhou, Q. Efficient decolorization of azo dye wastewater with polyaniline/graphene modified anode in microbial electrochemical systems. *J. Hazard. Mater.* **2022**, *421*, 126740. [[CrossRef](#)]
17. Mousavian, M.A.; Hosseini, S.; Ayati, B. Bioelectricity Generation and Decolorization of Reactive Blue 221 Using a Modified Cathode Dual-Chamber Microbial Fuel Cell. *Water* **2023**, *15*, 101. [[CrossRef](#)]

18. Chaijak, P.; Rakkan, T.; Paichaid, N.; Thipraksa, J.; Michu, P.; Sangkharak, K. Exploring Potential Aspect of Microbial Fuel Cell (MFC) for Simultaneous Energy, Polyhydroxyalkanoate (PHA) Production and Textile Wastewater (TW) Treatment. *J. Polym. Environ.* **2024**. [[CrossRef](#)]
19. Piskin, E.D.; Genc, N. Multi response optimization of waste activated sludge oxidation and azo dye reduction in microbial fuel cell. *Environ. Technol.* **2023**. [[CrossRef](#)]
20. Sun, J.; Cai, B.; Zhang, Y.; Peng, Y.; Chang, K.; Ning, X.; Liu, G.; Yao, K.; Wang, Y.; Yang, Z.; et al. Regulation of biocathode microbial fuel cell performance with respect to azo dye degradation and electricity generation via the selection of anodic inoculum. *Int. J. Hydrogen Energy* **2016**, *41*, 5141–5150. [[CrossRef](#)]
21. Biswas, A.; Chakraborty, S. Organics and coliform removal from low strength domestic wastewater using integrated constructed wetland-microbial fuel cell reactor with bioelectricity generation. *J. Clean. Prod.* **2023**, *408*, 137204. [[CrossRef](#)]
22. Patel, D.; Bapodra, S.L.; Madamwar, D.; Desai, C. Electroactive bacterial community augmentation enhances the performance of a pilot scale constructed wetland microbial fuel cell for treatment of textile dye wastewater. *Bioresour. Technol.* **2021**, *332*, 125088. [[CrossRef](#)] [[PubMed](#)]
23. Zhang, F.; Ge, Z.; Grimaud, J.; Hurst, J.; He, Z. Long-Term Performance of Liter-Scale Microbial Fuel Cells Treating Primary Effluent Installed in a Municipal Wastewater Treatment Facility. *Environ. Sci. Technol.* **2013**, *47*, 4941–4948. [[CrossRef](#)]
24. Cao, X.; Wang, H.; Li, X.-q.; Fang, Z.; Li, X.-n. Enhanced degradation of azo dye by a stacked microbial fuel cell-biofilm electrode reactor coupled system. *Bioresour. Technol.* **2017**, *227*, 273–278. [[CrossRef](#)]
25. Rathour, R.; Patel, D.; Shaikh, S.; Desai, C. Eco-electrogenic treatment of dyestuff wastewater using constructed wetland-microbial fuel cell system with an evaluation of electrode-enriched microbial community structures. *Bioresour. Technol.* **2019**, *285*, 121349. [[CrossRef](#)]
26. Li, X.; Dai, H.; Han, T.; Guo, Z.; Li, H.; Wang, X.; Abbasi, H.N. Construction of double tube granular sludge microbial fuel cell and its characteristics and mechanism of azo dye degradation. *Environ. Sci. Pollut. Res.* **2022**, *29*, 54606–54618. [[CrossRef](#)] [[PubMed](#)]
27. Thung, W.-E.; Ong, S.-A.; Ho, L.-N.; Wong, Y.-S.; Ridwan, F.; Oon, Y.-L.; Oon, Y.-S.; Lehl, H.K. A highly efficient single chambered up-flow membrane-less microbial fuel cell for treatment of azo dye Acid Orange 7-containing wastewater. *Bioresour. Technol.* **2015**, *197*, 284–288. [[CrossRef](#)]
28. Sonu, K.; Sogani, M.; Syed, Z. Integrated Constructed Wetland-Microbial Fuel Cell using Biochar as Wetland Matrix: Influence on Power Generation and Textile Wastewater Treatment. *Chemistryselect* **2021**, *6*, 8323–8328. [[CrossRef](#)]
29. Meng, F.; Song, M.; Chen, Y.; Wei, Y.; Song, B.; Cao, Q. Promoting adsorption of organic pollutants via tailoring surface physicochemical properties of biomass-derived carbon-attapulgite. *Environ. Sci. Pollut. Res.* **2021**, *28*, 11106–11118. [[CrossRef](#)]
30. Fang, J.H.; Dong, J.Y.; Li, C.C.; Chen, H.; Wang, L.F.; Lyu, T.S.; He, H.; Liu, J. Response of microbial community composition and function to emergent plant rhizosphere of a constructed wetland in northern China. *Appl. Soil Ecol.* **2021**, *168*, 104141. [[CrossRef](#)]
31. Han, Q.; Dong, W.; Wang, H.; Liu, T.; Sun, F.; Ying, Y.; Yan, X. Effects of coexisting anions on decolorization of azo dye X-3B by ferrate(VI) and a comparative study between ferrate(VI) and potassium permanganate. *Sep. Purif. Technol.* **2013**, *108*, 74–82. [[CrossRef](#)]
32. Guo, G.; Li, X.; Tian, F.; Liu, T.; Yang, F.; Ding, K.; Liu, C.; Chen, J.; Wang, C. Azo dye decolorization by a halotolerant consortium under microaerophilic conditions. *Chemosphere* **2020**, *244*, 125510. [[CrossRef](#)]
33. Prasad, A.S.A.; Rao, K.V.B. Aerobic biodegradation of azo dye Acid Black-24 by *Bacillus halodurans*. *J. Environ. Biol.* **2014**, *35*, 549–554.
34. Shahi, A.; Velayudhaperumal Chellam, P.; Verma, A.; Singh, R.S. A comparative study on the performance of microbial fuel cell for the treatment of reactive orange 16 dye using mixed and pure bacterial species and its optimization using response surface methodology. *Sustain. Energy Technol. Assess.* **2021**, *48*, 101667. [[CrossRef](#)]
35. Zhu, Y.; Cao, X.; Cheng, Y.; Zhu, T. Performances and structures of functional microbial communities in the mono azo dye decolorization and mineralization stages. *Chemosphere* **2018**, *210*, 1051–1060. [[CrossRef](#)] [[PubMed](#)]
36. Mao, Y.P.; Tao, Y.; Shen, Z.P.; Lei, Y.M.; Wang, W.H. Degradation Mechanism of Reactive Brilliant Red X-3B by Fenton Process. *Environ. Sci. Technol.* **2009**, *32*, 67–70.
37. He, Y.; Gao, J.-F.; Feng, F.-Q.; Liu, C.; Peng, Y.-Z.; Wang, S.-Y. The comparative study on the rapid decolorization of azo, anthraquinone and triphenylmethane dyes by zero-valent iron. *Chem. Eng. J.* **2012**, *179*, 8–18. [[CrossRef](#)]
38. Lu, J.; Ayele, B.A.; Liu, X.; Chen, Q. Electrochemical removal of RRX-3B in residual dyeing liquid with typical engineered carbonaceous cathodes. *J. Environ. Manag.* **2021**, *280*, 111669. [[CrossRef](#)] [[PubMed](#)]
39. Gao, X.; Zhang, L.; Sun, M.; Xiao, Y.; Su, J. Fast zero-order hydro-cracking reaction of X-3B over crystal Al-Fe alloys: Effect of electrochemical corrosion behaviors. *Mater. Des.* **2016**, *109*, 570–579. [[CrossRef](#)]
40. Wang, Z.; Zhang, Y.; Li, K.; Sun, Z.; Wang, J. Enhanced mineralization of reactive brilliant red X-3B by UV driven photocatalytic membrane contact ozonation. *J. Hazard. Mater.* **2020**, *391*, 122194. [[CrossRef](#)]
41. Ruan, X.-C.; Liu, M.-Y.; Zeng, Q.-F.; Ding, Y.-H. Degradation and decolorization of reactive red X-3B aqueous solution by ozone integrated with internal micro-electrolysis. *Sep. Purif. Technol.* **2010**, *74*, 195–201. [[CrossRef](#)]
42. Cao, Z.; Zhang, J.; Zhang, J.; Zhang, H. Degradation pathway and mechanism of Reactive Brilliant Red X-3B in electro-assisted microbial system under anaerobic condition. *J. Hazard. Mater.* **2017**, *329*, 159–165. [[CrossRef](#)] [[PubMed](#)]

43. Zhang, K.; Wu, X.; Wang, W.; Luo, H.; Chen, W.; Ma, D.; Mo, Y.; Chen, J.; Li, L. Effects of plant location on methane emission, bioelectricity generation, pollutant removal and related biological processes in microbial fuel cell constructed wetland. *J. Water Process Eng.* **2021**, *43*, 102283. [[CrossRef](#)]
44. Oon, Y.-L.; Ong, S.-A.; Ho, L.-N.; Wong, Y.-S.; Dahalan, F.A.; Oon, Y.-S.; Lehl, H.K.; Thung, W.-E. Synergistic effect of up-flow constructed wetland and microbial fuel cell for simultaneous wastewater treatment and energy recovery. *Bioresour. Technol.* **2016**, *203*, 190–197. [[CrossRef](#)]
45. Nishio, Y.; Nguyen, D.-T.; Taguchi, K. Urethane-based electrode material for microbial fuel cells. *Energy Rep.* **2023**, *9*, 66–73. [[CrossRef](#)]
46. Basu, A.; Manna, S.; Kumar Sil, A. A new electro-active bacterium, *Paraclostridium* sp. AKS46, converts waste efficiently into electricity in microbial fuel cell. *Chem. Eng. J.* **2023**, *475*, 145626. [[CrossRef](#)]
47. Guo, J.; Li, Q.; Gao, Q.; Shen, F.; Yang, Y.; Zhang, X.; Luo, H. Comparative study on the treatment of swine wastewater by VFCW-MFC and VFCW: Pollutants removal, electricity generation, microorganism community. *J. Environ. Manag.* **2023**, *342*, 118299. [[CrossRef](#)]
48. Song, Y.; Li, H.; Han, Y.; Lu, C.; Hou, Y.; Zhang, Y.; Guo, J. Landfill leachate as an additional substance in the Johannesburg-Sulfur autotrophic denitrification system in the treatment of municipal wastewater with low strength and low COD/TN ratio. *Bioresour. Technol.* **2020**, *295*, 122287. [[CrossRef](#)] [[PubMed](#)]
49. Zang, L.; Yang, X.-L.; Xu, H.; Deng, Y.-J.; Yue, Z.-X.; Song, H.-L. Alleviating membrane fouling by enhanced bioelectricity generation via internal reflux of sludge mixed liquor in microbial fuel cell-membrane bioreactor (MFC-MBR) coupling system. *J. Membr. Sci.* **2023**, *673*, 121495. [[CrossRef](#)]
50. Guo, H.; Xie, S.; Deng, H.; Geng, X.; Wang, P.; Huang, C.; Tang, S. Electricity production and bacterial communities of microbial fuel cell supplied with oily sludge. *Environ. Prog. Sustain. Energy* **2020**, *39*, e13409. [[CrossRef](#)]
51. Liu, S.-H.; Huang, W.-J.; Lin, C.-W.; Zhu, T.-J. Copper removal and microbial community analysis in a single medium sediment microbial fuel cell. *J. Water Process Eng.* **2021**, *44*, 102348. [[CrossRef](#)]
52. Liu, X.; Xu, Q.; Wang, D.; Wu, Y.; Yang, Q.; Liu, Y.; Wang, Q.; Li, X.; Li, H.; Zeng, G.; et al. Unveiling the mechanisms of how cationic polyacrylamide affects short-chain fatty acids accumulation during long-term anaerobic fermentation of waste activated sludge. *Water Res.* **2019**, *155*, 142–151. [[CrossRef](#)] [[PubMed](#)]
53. Amanze, C.; Zheng, X.; Anaman, R.; Wu, X.; Fosua, B.A.; Xiao, S.; Xia, M.; Ai, C.; Yu, R.; Wu, X.; et al. Effect of nickel (II) on the performance of anodic electroactive biofilms in bioelectrochemical systems. *Water Res.* **2022**, *222*, 118889. [[CrossRef](#)]
54. Rago, L.; Monpart, N.; Cortes, P.; Baeza, J.A.; Guisasola, A. Performance of microbial electrolysis cells with bioanodes grown at different external resistances. *Water Sci. Technol.* **2016**, *73*, 1129–1135. [[CrossRef](#)] [[PubMed](#)]
55. Ma, J.; Li, L.; Zhao, Q.; Yu, L.; Frear, C. Biomethane production from whole and extracted algae biomass: Long-term performance evaluation and *Microb.* community dynamics. *Renew. Energy* **2021**, *170*, 38–48. [[CrossRef](#)]
56. Guo, W.; Feng, J.; Song, H.; Sun, J. Simultaneous bioelectricity generation and decolorization of methyl orange in a two-chambered microbial fuel cell and bacterial diversity. *Environ. Sci. Pollut. Res.* **2014**, *21*, 11531–11540. [[CrossRef](#)] [[PubMed](#)]
57. Kook, L.; Kanyo, N.; Devenyi, F.; Bakonyi, P.; Rozsenberszki, T.; Belafi-Bako, K.; Nemestothy, N. Improvement of waste-fed bioelectrochemical system performance by selected electro-active microbes: Process evaluation and a kinetic study. *Biochem. Eng. J.* **2018**, *137*, 100–107. [[CrossRef](#)]
58. Wang, J.; Song, X.; Li, Q.; Bai, H.; Zhu, C.; Weng, B.; Yan, D.; Bai, J. Bioenergy generation and degradation pathway of phenanthrene and anthracene in a constructed wetland-microbial fuel cell with an anode amended with nZVI. *Water Res.* **2019**, *150*, 340–348. [[CrossRef](#)] [[PubMed](#)]
59. Gu, M.; Yin, Q.; Wang, Z.; He, K.; Wu, G. Color and nitrogen removal from synthetic dye wastewater in an integrated mesophilic hydrolysis/acidification and multiple anoxic/aerobic process. *Chemosphere* **2018**, *212*, 881–889. [[CrossRef](#)] [[PubMed](#)]
60. Ravadelli, M.; da Costa, R.E.; Lobo-Recio, M.A.; Vitor Akaboci, T.R.; Bassin, J.P.; Lapolli, F.R.; Belli, T.J. Anoxic/oxic membrane bioreactor assisted by electrocoagulation for the treatment of azo-dye containing wastewater. *J. Environ. Chem. Eng.* **2021**, *9*, 105286. [[CrossRef](#)]
61. Tao, M.; Jing, Z.; Tao, Z.; Luo, H.; Zuo, S.; Li, Y.-Y. Efficient nitrogen removal in microbial fuel cell-constructed wetland with corncobs addition for secondary effluent treatment. *J. Clean. Prod.* **2022**, *332*, 130108. [[CrossRef](#)]
62. Meng, L.; Xie, L.; Hirose, Y.; Nishiuchi, T.; Yoshida, N. Reduced graphene oxide increases cells with enlarged outer membrane of *Citri fermentans bremsense* and exopolysaccharides secretion. *Biosens. Bioelectron.* **2022**, *218*, 114754. [[CrossRef](#)] [[PubMed](#)]
63. Chen, Y.-Y.; Yang, F.-Q.; Xu, N.; Wang, X.-Q.; Xie, P.-C.; Wang, Y.-Z.; Fang, Z.; Yong, Y.-C. Engineered cytochrome fused extracellular matrix enabled efficient extracellular electron transfer and improved performance of microbial fuel cell. *Sci. Total Environ.* **2022**, *830*, 154806. [[CrossRef](#)] [[PubMed](#)]

Disclaimer/Publisher's Note: The statements, opinions and data contained in all publications are solely those of the individual author(s) and contributor(s) and not of MDPI and/or the editor(s). MDPI and/or the editor(s) disclaim responsibility for any injury to people or property resulting from any ideas, methods, instructions or products referred to in the content.